Reliable operation in high-mobility indium oxide thin film transistors

Prashant R. Ghediya, Yusaku Magari*, Hikaru Sadahira, Takashi Endo, Mamoru Furuta, Yuqiao Zhang, Yasutaka Matsuo & Hiromichi Ohta*

P. R. Ghediya, Y. Magari, T. Endo, Y. Matsuo, H. Ohta
Research Institute for Electronic Science, Hokkaido University, N20W10, Kita, Sapporo 001-0020, Japan
E-mail: yusaku.magari@es.hokudai.ac.jp, hiromichi.ohta@es.hokudai.ac.jp

H. Sadahira
Graduate School of Information Science and Technology, Hokkaido University, N20W10, Kita, Sapporo 001-0020, Japan

M. Furuta
School of Environmental Science and Engineering, Kochi University of Technology, Kami, Kochi, 782-8502, Japan

Y. Zhang
Institute of Quantum and Sustainable Technology, Jiangsu University, Zhenjiang 212013, China

Abstract

Transparent oxide semiconductors (TOSs) based thin-film transistors (TFTs) that exhibit higher field effect mobility (μ_{FE}) are highly required toward the realization of next-generation displays. Among numerous types of TOS-TFTs, In_2O_3-based TFTs are the front-running candidate because they exhibit the highest μ_{FE} ~100 cm^2 V^{-1} s^{-1}. However, the device operation of In_2O_3 TFTs is unreliable; a large voltage shift occurs especially when negative gate bias is applied due to adsorption/desorption of gas molecules. Although passivation of the TFTs is used to overcome such instability, previously proposed passivation materials did not improve the reliability. Here, we show that the In_2O_3 TFTs passivated with Y_2O_3 and Er_2O_3 films are highly reliable and do not show threshold voltage shifts when applying gate

bias. We applied positive and negative gate bias to the In_2O_3 TFTs passivated with various insulating oxides and found that only the In_2O_3 TFTs passivated with Y_2O_3 and Er_2O_3 films did not exhibit threshold voltage shifts. We observed that only the Y_2O_3 grew heteroepitaxially on the In_2O_3 crystal. This would be the origin of the high reliability of the In_2O_3 TFTs passivated with Y_2O_3 and Er_2O_3 films. This finding accelerates the development of next-generation displays using high-mobility In_2O_3 TFTs.

Introduction

Transparent oxide semiconductor (TOS)-based thin-film transistors (TFTs) have been widely used as the backplane of flat panel displays (FPDs), such as liquid crystal displays (LCDs) and organic light-emitting diodes (OLEDs)[1-4]. Their performance is characterized by the field effect mobility (μ_{FE}). The μ_{FE} of amorphous $InGaZnO_4$ (a-IGZO) TFTs[5,6], which has been commercialized, is ~10 cm^2 V^{-1} s^{-1}. However, even higher-definition (*e.g.,* super high definition, SHD) FPDs that are operatable at higher frequencies (>240 Hz) demand μ_{FE} ~100 cm^2 V^{-1} s^{-1}, one order of magnitude higher than that of a-IGZO TFTs[7-10]. Therefore, numerous efforts have been made thus far to find good TOSs that show high μ_{FE}.[11-17] Among numerous reports on TOS-TFTs, Magari *et al*. reported that hydrogen incorporated In_2O_3 TFTs stand out high μ_{FE} ~140 cm^2 V^{-1} s^{-1} [17]. Although the influence of the grain boundary scattering of electrons in polycrystalline materials is a major concern, the low-temperature (~300 °C) solid-phase crystallization technique is effective in increasing the lateral grain size and mobility and reducing the subgap defects in In_2O_3 films. Thus, In_2O_3 TFTs have been front-running candidates.

However, there is a serious drawback to the operation of In_2O_3 TFTs, which makes them inappropriate for practical applications. In real applications, the TFT operation must be stable against gate bias applications. Current In_2O_3 TFTs exhibit a large negative threshold voltage (V_{th}) shift when a negative gate bias stress is applied (**Fig. 1a**). In the case of a-IGZO TFTs, the origin of the V_{th} shift is mainly gas adsorption/desorption, and such a V_{th} shift is suppressed by covering the active material layer (passivation).[18,19] As a passivation material, a-SiO_2 is widely used, and the V_{th} shift of a-IGZO TFTs is successfully suppressed.[20-24] Therefore, Magari *et al*.[17] deposited a-SiO_2 film as the passivation layer of the In_2O_3 TFTs, but the resultant TFTs showed a large V_{th} shift (~5 V) after applying negative gate bias stress. Thus, a-SiO_2 passivation is useless in improving the reliability of In_2O_3 TFTs.

To overcome this difficulty and realize ideal In$_2$O$_3$ TFTs with reliability (**Fig. 1b**), we passivated the In$_2$O$_3$ active layer surface of In$_2$O$_3$ TFTs with various insulating oxides, as schematically shown in **Fig. 1c**, including HfO$_2$, Al$_2$O$_3$, Y$_2$O$_3$, Er$_2$O$_3$, Gd$_2$O$_3$, Yb$_2$O$_3$, Sm$_2$O$_3$, and Nd$_2$O$_3$. We selected amorphous HfO$_2$ and Al$_2$O$_3$ films because they are often used as the passivation layers for TOS TFTs.[25-27] Further, we selected Ln_2O$_3$ (Ln: Lantanoid, Ln = Y, Er, Gd, Yb, Sm, and Nd) because the ionic radius of the Ln^{3+} is close to that of In^{3+} and the crystal structure of Ln_2O$_3$ (C-rare earth structure: Ln = Y, Er, Gd, and Yb, B-rare earth structure: Ln = Sm, A-rare earth structure: Ln = Nd) is similar to that of In$_2$O$_3$ (C-rare earth structure). Note that Nomura et al. reported that Y$_2$O$_3$ passivation effectively improves the reliability of a-IGZO TFTs.[28] We expected that heteroepitaxial growth of Ln_2O$_3$ would occur on In$_2$O$_3$[29] and the reliability would be improved. Interestingly, only the In$_2$O$_3$ TFTs passivated with Y$_2$O$_3$ and Er$_2$O$_3$ films showed excellent reliability, whereas those passivated with all other insulating oxides exhibited poor reliability.

Here, we show that In$_2$O$_3$-TFTs passivated with Y$_2$O$_3$ and Er$_2$O$_3$ films are highly reliable; the V_{th} shifts are negligible after applying a gate bias. We applied positive and negative gate biases to In$_2$O$_3$ TFTs passivated with various insulating oxides and found that only the In$_2$O$_3$ TFTs passivated with Y$_2$O$_3$ and Er$_2$O$_3$ films did not exhibit V_{th} shifts. We observed that only Y$_2$O$_3$ grew heteroepitaxially on the In$_2$O$_3$ crystals. This could be the origin of the high reliability of the In$_2$O$_3$ TFTs passivated with Y$_2$O$_3$ and Er$_2$O$_3$. The present findings are expected to accelerate the development of next-generation displays using In$_2$O$_3$ TFTs showing high μ_{FE}.

Results and discussion

We fabricated bottom-gate top-contact In$_2$O$_3$ TFTs on ITO-coated alkali-free glass substrates. The ITO was used as the bottom gate electrode. We used a 100-nm-thick AlO$_x$ film as a gate insulator. The dielectric permittivity (ε_r) and capacitance (C_i) of the AlO$_x$ films were 8 and 70 nF cm^{-2}, respectively. We deposited a 5-nm-thick amorphous In$_2$O$_3$ film on the AlO$_x$ film at room temperature through a stencil mask. The multilayer film was heated at 300 °C in air for 0.5 h to crystalize the In$_2$O$_3$ active layer. Then, 100-nm-thick indium tin oxide (ITO) source/drain electrodes were deposited through a stencil mask. The channel length (L) and width (W) were 200 and 400 µm, respectively. After that, ~50-nm-thick HfO$_2$, Al$_2$O$_3$, and Ln_2O$_3$ (Ln: Lanthanoid = Y, Er, Gd, Yb, Sm, and Nd) films were deposited as the passivation layer through a stencil mask without substrate heating. Finally, the TFT was thermally

annealed at 370 °C in air for 0.5 h. After the thermal annealing, Ln_2O_3 films were polycrystalline whereas HfO_2 and Al_2O_3 films remained amorphous (**Fig. S1**).

The transistor characteristics were measured using a semiconductor device analyzer (B1500A, Agirent) by applying a constant drain voltage (V_d) of 5 V. We measured the transfer characteristics after applying a positive gate bias stress (PBS; $V_g = +20$ V, electric field $E = 2$ MV cm^{-1}) and a negative gate bias stress (NBS; $V_g = -20$ V, electric field $E = -2$ MV cm^{-1}) for up to 5000 s to the TFTs at room temperature in air. Details of our TFT fabrication and measurement are described in the **Method** section.

First, we measured the transistor characteristics of the In_2O_3 TFTs without a passivation layer (**Fig. 2**). The TFT showed excellent transistor characteristics before applying bias stress (Holding time = 0 s in **Fig. 2a**); the field effect mobility (μ_{FE}) of ~85 cm^2 V^{-1} s^{-1}, threshold voltage (V_{th}) of -3.2 V, subthreshold swing of ~0.22 V decade^{-1}, and TFT did not show a hysteresis behavior. However, after applying PBS for 5000 s, a positive V_{th} shift of $+1$ V was observed (**Fig. 2a**). After applying NBS for 5000 s, the negative V_{th} shift of -10 V occurred (**Fig. 2b**). These results demonstrate that the polycrystalline In_2O_3 TFTs without a passivation layer are unreliable.

Then, we measured the transistor characteristics of the In_2O_3 TFTs with passivation layers (**Figs. S2−S9**). Although HfO_2 and Al_2O_3 play as good passivation materials for a-IGZO TFTs, the In_2O_3 TFTs passivated with HfO_2 (**Fig. S2**) and Al_2O_3 (**Fig. S3**) show a large V_{th} shift especially after NBS (HfO_2: -4.4 V, Al_2O_3: -7.0 V), showing unreliability of the TFTs. Importantly, the In_2O_3 TFTs passivated with the Y_2O_3 (**Fig. S4**) and Er_2O_3 (**Fig. S5**) films exhibited excellent reliability, and the V_{th} shifts were negligible after both PBS and NBS. The TFTs passivated with the Gd_2O_3 (**Fig. S6**) and Yb_2O_3 (**Fig. S7**) films showed good reliability. However, the TFTs passivated with the Sm_2O_3 (**Fig. S8**) and Nd_2O_3 (**Fig. S9**) films exhibited a large V_{th} shift after both PBS and NBS. The V_{th} shift results after 5000 s application of PBS and NBS are summalized in **Figs. 2c** and **2d**, respectively. From these results, we conclude that the Y_2O_3 and Er_2O_3 films are excellent passivation materials for realizing reliable In_2O_3 TFTs.

We also realized that the performance degradation of the In_2O_3 TFTs did not occur using Y_2O_3 and Er_2O_3 film passivation. **Figure 3** shows the bias stress time dependence of the μ_{FE}

4

(**Figs. 3a** and **3b**) and subthreshold swing (**Figs. 3c** and **3d**) under PBS and NBS. The μ_{FE} and subthreshold swing values of the In_2O_3 TFT without passivation drastically changed with stress time, showing unreliability. In contrast, the μ_{FE} and subthreshold swing values of the In_2O_3 TFTs passivated with Y_2O_3 and Er_2O_3 are highly stable against the bias stress application. The μ_{FE} of the Y_2O_3 passivated TFT was ~78 cm^2 V^{-1} s^{-1} and that of the Er_2O_3 passivated TFT was ~70 cm^2 V^{-1} s^{-1}. The subthreshold swing of both TFTs was ~0.1 V decade^{-1}. These results demonstrate that a reliable device operation in In_2O_3 TFTs can be achieved using Y_2O_3 and Er_2O_3 films as passivation layers.

Here, we discuss the origin of the reliability of In_2O_3 TFT passivated with Y_2O_3 and Er_2O_3 films. We hypothesized that the Y_2O_3 and Er_2O_3 films grew heteroepitaxially on the In_2O_3 films because these oxides have the same crystal structure as In_2O_3 (C-rare-earth structure). To confirm this, we prepared ~100-nm-thick rare-earth oxide (Ln_2O_3) (Ln = Y, Nd, and Sm) films on (111)-oriented 10%-Sn-doped In_2O_3 epitaxial films using the same procedure as for passivation layer fabrication. **Figure 4** shows cross-sectional high-angle annular dark-field (HAADF) scanning transmission electron microscopy (STEM) images of the Ln_2O_3 films. Although several strong contrasts, indicated by yellow arrows owing to cracks, were observed in the Sm_2O_3 and Nd_2O_3 films, such microstructures were not observed in the Y_2O_3 film. Weak contrasts were observed around the heterointerfaces between Sm_2O_3/In_2O_3 and Nd_2O_3/In_2O_3. Interestingly, the lattice structures of Y_2O_3 are visible together with that of In_2O_3 in the magnified HAADF-STEM images (**Figs. 5a** and **5b**), indicating that heteroepitaxial growth occurred. In contrast, the magnified images of the heterointerfaces of the Sm_2O_3/In_2O_3 (**Fig. 5c**) and Nd_2O_3/In_2O_3 (**Fig. 5d**) visualize the existence of an amorphous structure, which is the origin of the contrast around the heterointerfaces. These results reveal that heteroepitaxial growth of the passivation materials is the key to improving the reliability of In_2O_3 TFTs.

To further clarify the origin that heteroepitaxial growth of Y_2O_3 occurred on In_2O_3, we plotted the relationship between the ionic radius and metal−oxygen bond (M−O) length in various Ln_2O_3 (**Fig. 6a**). Ln_2O_3 has three different crystal structures (*i.e.* C-, B-, and A-type) depending on the ionic radius. The C-type structures (Yb_2O_3, Er_2O_3, Y_2O_3, and Gd_2O_3) are cubic bixbyite and have the same crystal structure as In_2O_3 with an ionic radius of 0.80 Å. As shown in light blue in **Fig. 6a**, the M−O lengths of Er−O and Y−O are close to In−O. Therefore heteroepitxial growth of Y_2O_3 occurred on In_2O_3. We also plotted the V_{th} shifts

after PBS and NBS of the In_2O_3 TFTs as a function of the difference in $M-O$ length from In$-$O length ($\Delta l_{(M-O)-(In-O)}$) (**Fig. 6b**). The V_{th} shifts are significant for both PBS and NBS when the shortest $\Delta l_{(M-O)-(In-O)}$ of the passivation layer exceeds 0.15 Å (Gd_2O_3). In contrast, the V_{th} shifts are negligible when the shortest $\Delta l_{(M-O)-(In-O)}$ is below 0.10 Å (Y_2O_3 and Er_2O_3). These results indicate that the bias stress stability is highly dependent on the $\Delta l_{(M-O)-(In-O)}$ of the passivation layer.

Finally, we like to discuss the reason why the heteroepitaxial growth of the passivation material effectively improves the bias stress stability of In_2O_3 TFTs. Generally, gas molecules (O_2, H_2O, CO_2, etc.) are adsorbed on the surface of oxide semiconductors such as IGZO[18,19], In_2O_3[30], and SnO_2[31,32] and drastically suppress the conductivity of the oxide semiconductors. We performed thermal desorption spectroscopy (TDS) measurements of the In_2O_3 films to determine the absorbed gas molecules (**Fig. S10**). We confirmed that the H_2 and CO desorption are negligible while small desorption of O_2 and large desorption of H_2O occur from In_2O_3 film at relatively low temperatures (~60 °C). These results suggest that the desorption of the OH^- ion occurs during the NBS test of the In_2O_3 TFTs and the ion leaves carrier electrons in the In_2O_3 film. Thus, NBS increases the residual carrier electron concentration, resulting in significant V_{th} shifts toward the negative side after NBS. Consequently, the heteroepitaxially grown Y_2O_3 and Er_2O_3 passivation layers would effectively prevent the desorption of OH^- ions from the In_2O_3 films. These findings are expected to accelerate the development of next-generation FPDs using In_2O_3 TFTs.

Summary
We demonstrated a key interface engineering strategy to stabilize the device operation of high-mobility In_2O_3 TFTs by applying Y_2O_3 and Er_2O_3 films as a passivation layer. We applied positive and negative gate bias to the In_2O_3 TFTs passivated with various insulating oxides and found that only the In_2O_3 TFTs passivated with Y_2O_3 and Er_2O_3 films did not exhibit degradations in V_{th}, μ_{FE}, and subthreshold swing. We observed that only the Y_2O_3 films grew heteroepitaxially on the In_2O_3 crystals. Consequently, protecting the In_2O_3 back-channel surface with Ln_2O_3 films, featuring similar crystal structure and $M-O$ length as In_2O_3, prevents the desorption/absorption of gas molecules. This could be the origin of the high reliability of the In_2O_3 TFTs passivated with Y_2O_3 and Er_2O_3. These findings are expected to accelerate the development of next-generation displays using high-mobility In_2O_3 TFTs.

Methods

Fabrication of In$_2$O$_3$ TFTs

Bottom-gate top-contact In$_2$O$_3$ TFTs were fabricated on ITO-coated alkali-free glass substrates (EAGLE XG®, Corning®). First, a 100-nm-thick AlO$_x$ gate insulator was deposited on the substrate by atomic layer deposition. The dielectric permittivity (ε_r) and capacitance (C_i) of the AlO$_x$ films were 8 and 70 nF cm^{-2}, respectively. Subsequently, a 5-nm-thick In$_2$O$_3$ film was deposited on the AlO$_x$ film via pulsed laser deposition (PLD) under an oxygen pressure of 3 Pa at room temperature through a stencil mask. The multilayer film was annealed at 300 °C in ambient air for 30 min. Subsequently, 100-nm-thick indium tin oxide (ITO) source/drain electrodes were deposited by PLD through a stencil mask. The channel length (L) and width (W) were 200 and 400 µm, respectively. Subsequently, ~50-nm-thick HfO$_2$, Al$_2$O$_3$, and rare-earth oxide (Ln_2O$_3$) (Ln: Lanthanoid = Y, Er, Gd, Yb, Sm, and Nd) films were deposited via PLD through a stencil mask without substrate heating. These films served as passivation layers. Finally, the TFT was thermally annealed at 370 °C in air for 30 min.

Reliability tests of the In$_2$O$_3$ TFTs

The transfer characteristics of the In$_2$O$_3$ TFTs were measured in the dark using a semiconductor device analyzer (B1500A, Agilent). Positive gate bias stress (PBS, V_g = +20 V) and negative gate bias stress (NBS, V_g = −20 V) tests were conducted for In$_2$O$_3$ TFTs for 5000 s at room temperature in air ambient. The field effect mobility (μ_{FE}) was calculated from the linear transfer characteristics at a drain voltage (V_d) of 5 V using equation (1).

$$\mu_{FE} = \frac{g_m}{C_i \frac{W}{L} V_d}, \qquad (1)$$

where g_m is the transconductance, C_i is the oxide capacitance of the gate insulator (70 nF cm^{-2} for AlO$_x$), and V_d is the drain voltage. The subthreshold swing was extracted from V_g, which required an increase in the drain current (I_d) from 1 to 10 pA.

Microstructure analyses of the Ln_2O$_3$ films

To visualize detailed microstructures, including lattice images, single-crystalline In$_2$O$_3$ substrates are necessary. First, we prepared atomically flat 10%-Sn-doped In$_2$O$_3$ epitaxial films on (111)-oriented YSZ single crystal substrates by PLD. Details of the 10%-Sn-doped In$_2$O$_3$ epitaxial film growth have been published elsewhere[29]. We then deposited Ln_2O$_3$ (Ln = Y, Sm, and Nd) films on the In$_2$O$_3$ epitaxial films by PLD under the same conditions used for

TFT fabrication. Finally, the bilayer films were thermally annealed at 370 °C in air for 30 min. The cross-sectional microstructures of the Ln_2O_3 films were observed using a high-angle annular dark-field (HAADF) scanning transmission electron microscope (STEM; JEM-ARM 200CF, JEOL Co. Ltd.) operated at 200 keV. The incident e-beam direction was $<1\bar{1}0>$ In_2O_3.

Thermal desorption spectroscopy of the In_2O_3 films

The desorption gases (H_2, H_2O, CO, and O_2) from the In_2O_3 film were measured by thermal desorption spectroscopy (TDS, TDS1200II, ESCO) with a raising temperature rate of 60 °C min^{-1}. The base pressure of the system was 5×10^{-7} Pa. Si substrates with 100-nm-thick thermally grown SiO_2 were used for the TDS measurements.

Supplementary Information

Supplementary Figs. S1−S10 and Table S1

References

1   Kamiya, T. & Hosono, H. Material Characteristics and Applications of Transparent Amorphous Oxide Semiconductors. *NPG Asia Mater.* **2**, 15-22 (2010).

2   Fortunato, E., Barquinha, P. & Martins, R. Oxide Semiconductor Thin-Film Transistors: A Review of Recent Advances. *Adv. Mater.* **24**, 2945-2986 (2012).

3   Hosono, H. How we made the IGZO transistor. *Nat. Electron.* **1**, 428-428 (2018).

4   *Amorphous Oxide Semiconductors: IGZO and Related Materials for Display and Memory.* (Wiley, 2022).

5   Nomura, K. *et al.* Room-temperature fabrication of transparent flexible thin-film transistors using amorphous oxide semiconductors. *Nature* **432**, 488-492 (2004).

6   Kim, Y. H. *et al.* Flexible metal-oxide devices made by room-temperature photochemical activation of sol-gel films. *Nature* **489**, 128-U191 (2012).

7   Kwon, J. Y. & Jeong, J. K. Recent progress in high performance and reliable n-type transition metal oxide-based thin film transistors. *Semicond. Sci. Technol.* **30**, 024002 (2015).

8   Hara, Y. *et al.* IGZO-TFT technology for large-screen 8K display. *J. Soc. Inf. Display* **26**, 169-177 (2018).

9   Hendy, I., Brewer, J. & Muir, S. Development of High-Performance IGZO Backplanes for Displays. *Information Display* **38**, 60-68 (2022).

10   Kim, T. *et al.* Progress, Challenges, and Opportunities in Oxide Semiconductor Devices: A Key Building Block for Applications Ranging from Display Backplanes to 3D Integrated Semiconductor Chips. *Adv. Mater.* **35**, e2204663 (2023).

11   Dehuff, N. L., Kettenring, E. S., Hong, D., Chiang, H. Q. & Wager, J. F. Transparent thin-film transistors with zinc indium oxide channel layer. *J. Appl. Phys.* **97**, 064505 (2005).

12   Cho, S. H. *et al.* Highly Stable, High Mobility Al:SnZnInO Back-Channel Etch Thin-Film Transistor Fabricated Using PAN-Based Wet Etchant for Source and Drain Patterning. *IEEE Trans. Electron Dev.* **62**, 3653-3657 (2015).

13   Sheng, J. *et al.* Amorphous IGZO TFT with High Mobility of ~70 cm^2/Vs via Vertical Dimension Control Using PEALD. *ACS Appl. Mater. Interfaces* **11**, 40300-40309 (2019).

14   Shiah, Y. S. *et al.* Mobility-stability trade-off in oxide thin-film transistors. *Nat. Electron.* **4**, 800-807 (2021).

15   Lee, J. *et al.* Hydrogen-Doping-Enabled Boosting of the Carrier Mobility and Stability in Amorphous IGZTO Transistors. *ACS Appl. Mater. Interfaces* **14**, 57016-57027 (2022).

16   Rabbi, M. H. *et al.* Polycrystalline InGaO Thin-Film Transistors with Coplanar Structure Exhibiting Average Mobility of approximately 78 cm^2 V^{-1} s^{-1} and Excellent Stability for Replacing Current Poly-Si Thin-Film Transistors for Organic Light-Emitting Diode Displays. *Small Methods* **6**, e2200668 (2022).

17   Magari, Y., Kataoka, T., Yeh, W. C. & Furuta, M. High-mobility hydrogenated polycrystalline In$_2$O$_3$ (In$_2$O$_3$:H) thin-film transistors. *Nat. Commun.* **13**, 1078 (2022).

18   Jeong, J. K., Yang, H. W., Jeong, J. H., Mo, Y. G. & Kim, H. D. Origin of threshold voltage instability in indium-gallium-zinc oxide thin film transistors. *Appl. Phys. Lett.* **93**, 123508 (2008).

19   Conley, J. F. Instabilities in Amorphous Oxide Semiconductor Thin-Film Transistors. *IEEE Trans. Dev. Mater. Reliability* **10**, 460-475 (2010).

20   Chen, T. C. *et al.* Light-induced instability of an InGaZnO thin film transistor with and without SiO$_x$ passivation layer formed by plasma-enhanced-chemical-vapor-deposition. *Appl. Phys. Lett.* **97**, 192103 (2010).

21   Chowdhury, M. D. H. *et al.* Effect of SiO$_2$ and SiO$_2$/SiN$_x$ Passivation on the Stability of Amorphous Indium-Gallium Zinc-Oxide Thin-Film Transistors Under High Humidity. *IEEE Trans. Electron Dev.* **62**, 869-874 (2015).

22   Zheng, L. L. *et al.* High-Performance Unannealed a-InGaZnO TFT With an Atomic-Layer-Deposited SiO$_2$ Insulator. *IEEE Electron. Dev. Lett.* **37**, 743-746 (2016).

23   Aman, S. G. M., Koretomo, D., Magari, Y. & Furuta, M. Influence of Deposition Temperature and Source Gas in PE-CVD for SiO$_2$ Passivation on Performance and Reliability of In-Ga-Zn-O Thin-Film Transistors. *IEEE Trans. Electron Dev.* **65**, 3257-3263 (2018).

24   Xiao, X. *et al.* Room-Temperature-Processed Flexible Amorphous InGaZnO Thin Film Transistor. *ACS Appl. Mater. Interfaces* **10**, 25850-25857 (2018).

25   Yang, S. *et al.* Improvement in the photon-induced bias stability of Al-Sn-Zn-In-O thin film transistors by adopting AlO$_x$ passivation layer. *Appl. Phys. Lett.* **96**, 213511 (2010).

26   Ko, Y. *et al.* The effects of a HfO$_2$ buffer layer on Al$_2$O$_3$-passivated indium-gallium-zinc-oxide thin film transistors. *Phys. Status Solidi. RRL* **5**, 403-405 (2011).

27   Nomura, K., Kamiya, T. & Hosono, H. Stability and high-frequency operation of amorphous In-Ga-Zn-O thin-film transistors with various passivation layers. *Thin Solid Films* **520**, 3778-3782 (2012).

28   Nomura, K., Kamiya, T. & Hosono, H. Highly stable amorphous In-Ga-Zn-O thin-film transistors produced by eliminating deep subgap defects. *Appl. Phys. Lett.* **99**, 053505 (2011).

29   Ohta, H. *et al.* Transparent organic thin-film transistor with a laterally grown non-planar phthalocyanine channel. *Adv. Mater.* **16**, 312 (2004).

30   Gurlo, A. *et al.* Grain size control in nanocrystalline In_2O_3 semiconductor gas sensors. *Sensor Actuat. B* **44**, 327-333 (1997).

31   Yamazoe, N. New Approaches for Improving Semiconductor Gas Sensors. *Sensor Actuat B-Chem* **5**, 7-19 (1991).

32   Liang, D. D., Zhang, Y. Q., Hai, J. C. & Ohta, H. Electric field thermopower modulation analyses of the operation mechanism of transparent amorphous SnO_2 thin-film transistor. *Appl. Phys. Lett.* **116**, 143503 (2020).
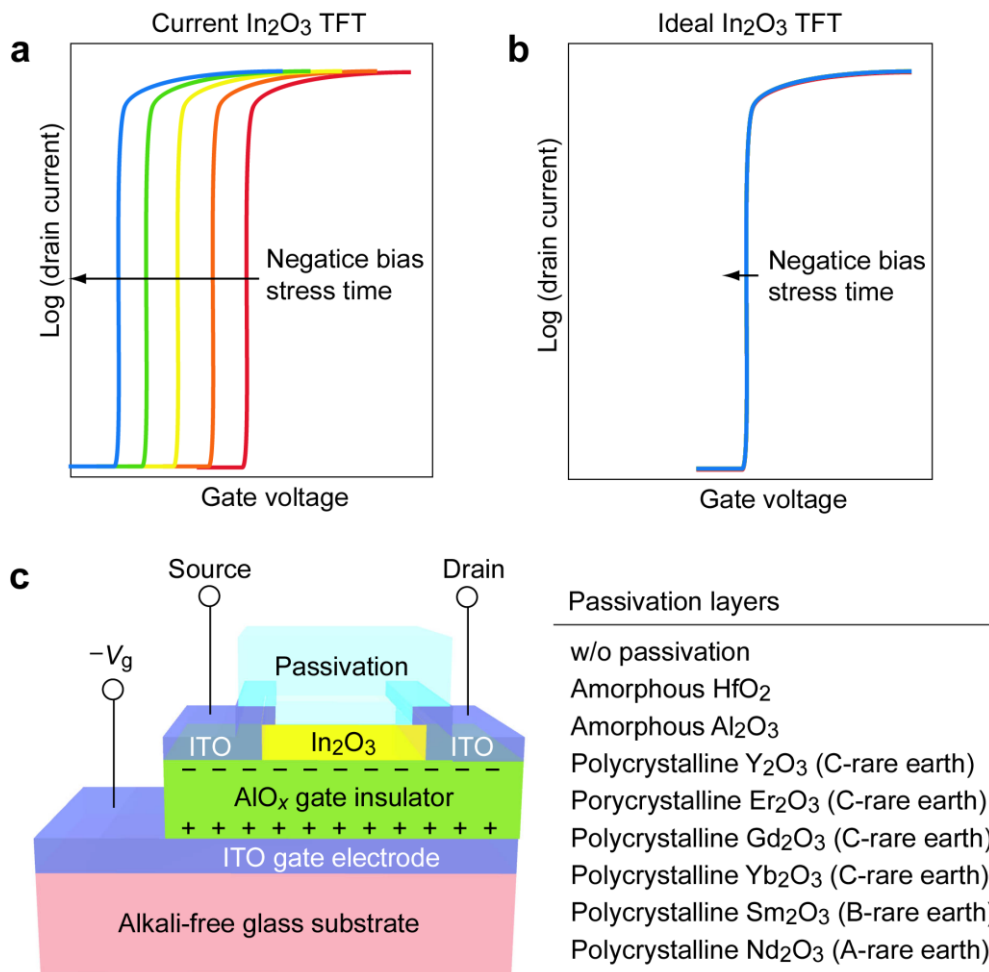
Figure 1: Passivation strategy towards the improvement of reliability of high-mobility In$_2$O$_3$ TFTs.
Schematic transistor characteristics after applying bias stress of (a) current and (b) ideal In$_2$O$_3$ TFTs. Current In$_2$O$_3$ TFTs show high-mobility (~100 cm^2 V^{-1} s^{-1}). However, there is a major drawback; current In$_2$O$_3$ TFTs show large voltage shifts upon applying bias stress. Therefore, ideal In$_2$O$_3$ TFTs that show good reliability are in high demand. (c) Passivation strategy. Schematic illustration of a bottom-gate top-contact type In$_2$O$_3$ TFT with a surface passivation layer. ~50-nm-thick HfO$_2$, Al$_2$O$_3$, Y$_2$O$_3$, Er$_2$O$_3$, Gd$_2$O$_3$, Yb$_2$O$_3$, Sm$_2$O$_3$, and Nd$_2$O$_3$ films were tested as the surface passivation layer. C-rare earth oxides were mainly chosen because their crystal structures are the same as those of In$_2$O$_3$. HfO$_2$ and Al$_2$O$_3$ films were amorphous, whereas the other oxide films were polycrystalline.
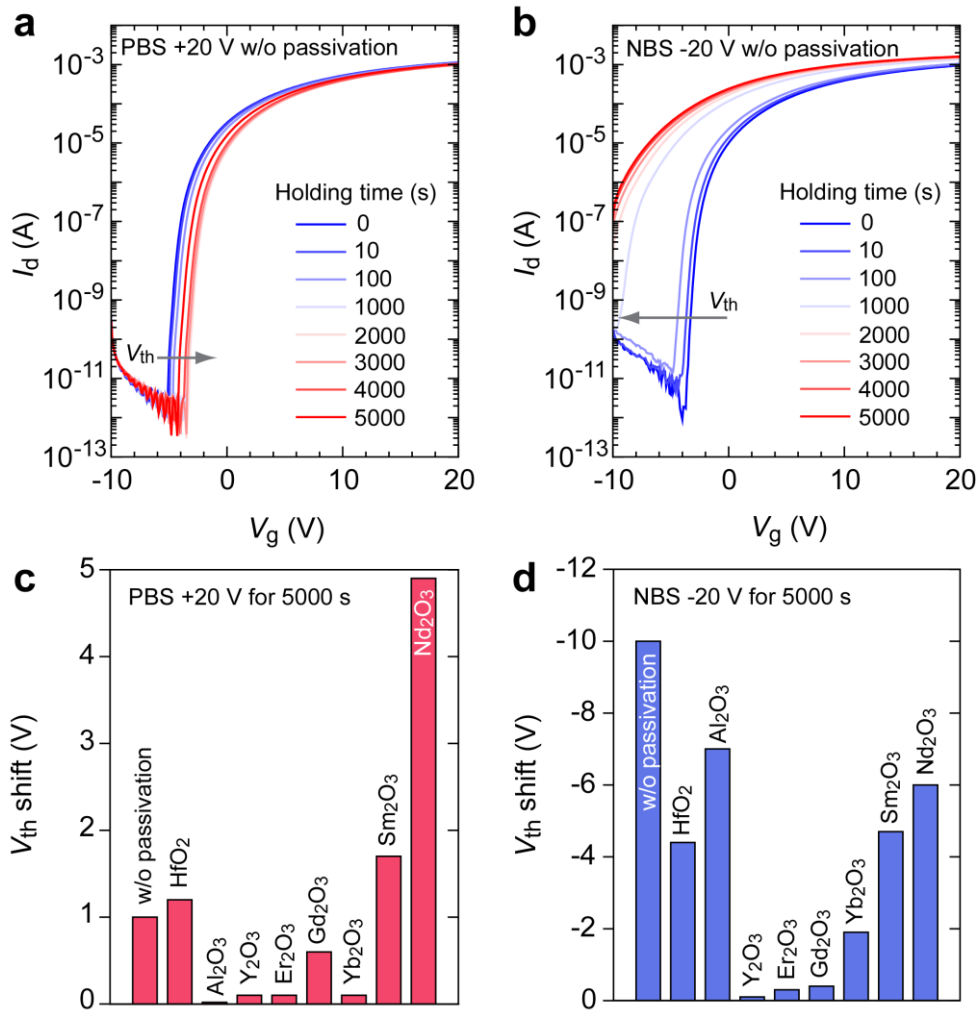
Figure 2: Bias stress test results of the In₂O₃ TFTs with various passivation layers.
(a, b) Changes in transfer characteristics of the In_2O_3 TFTs without a passivation layer under
(a) PBS (+20 V) and (b) NBS (−20 V). Threshold voltage (V_{th}) shifts of +1 V after 5000 s
PBS and −10 V after 5000 s NBS were observed. This is the major drawback of In_2O_3 TFTs.
(c, d) V_{th} shifts of the In_2O_3 TFTs with various passivation layers after (c) PBS and (d) NBS
for 5000 s extracted from **Figures S1−S8**. The In_2O_3 TFTs passivated with polycrystalline
Y_2O_3 and Er_2O_3 films show negligible V_{th} shift under both PBS and NBS. The Gd_2O_3 and
Yb_2O_3 film passivation results in a small V_{th} shift after the PBS and NBS. Overall, the In_2O_3
TFTs passivated with C-rare earth oxides show small V_{th} shifts after PBS and NBS for 5000 s.
Conversely, In_2O_3 TFTs passivated with HfO_2, Al_2O_3, Sm_2O_3, and Nd_2O_3 films still show
large V_{th} shifts after NBS, indicating that these films are not effective as the passivation layers
for In_2O_3 TFTs.
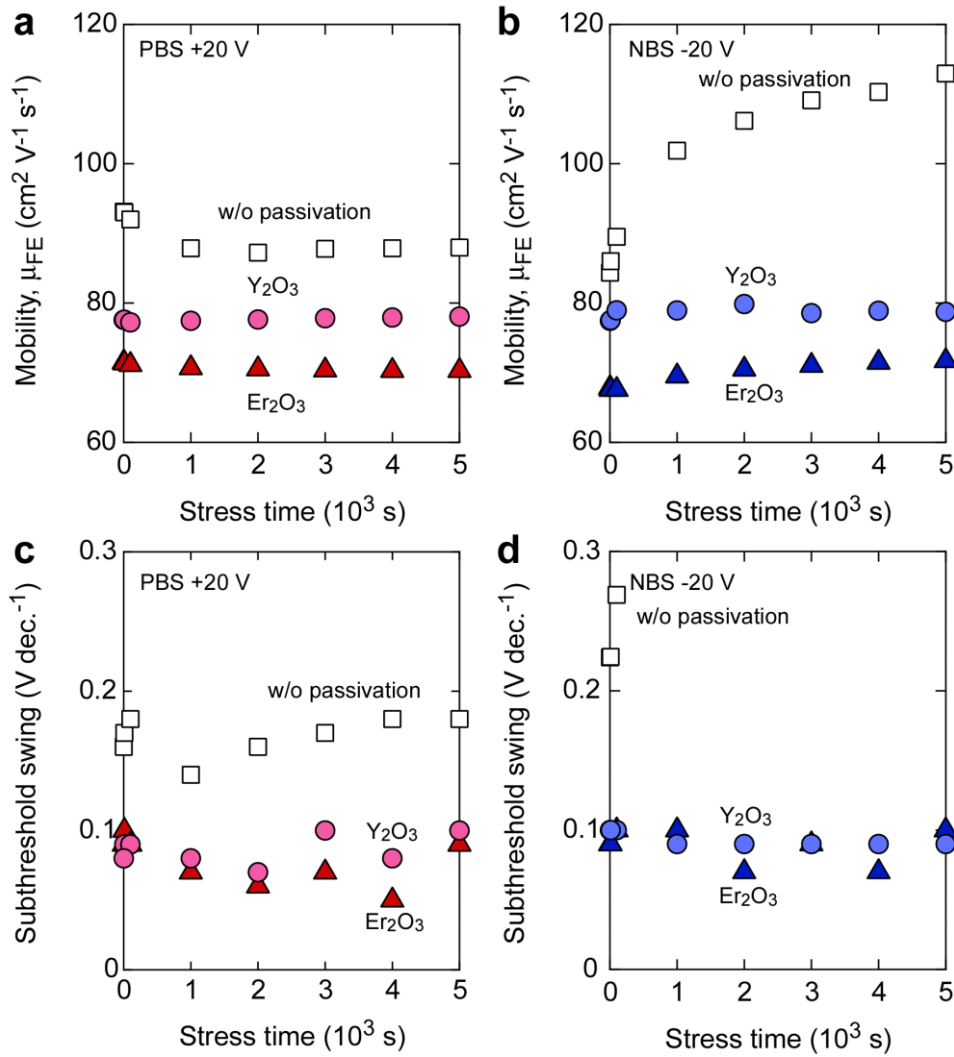
Figure 3: Effects of the Y_2O_3 and Er_2O_3 films passivation on the transistor characteristics of the In_2O_3 TFTs.

(a, b) Field effect mobility (μ_{FE}). (c, d) Subthreshold swing. The In_2O_3 TFT without passivation exhibits unreliability; Both μ_{FE} and subthreshold swings change with the stress time. In contrast, the In_2O_3 TFTs passivated with Y_2O_3 and Er_2O_3 are highly reliable; the μ_{FE} and subthreshold swing are stable against the bias stress application. The μ_{FE} of the Y_2O_3 passivated TFT is ~78 cm^2 V^{-1} s^{-1} and that of the Er_2O_3 passivated TFT is ~70 cm^2 V^{-1} s^{-1}. The subthreshold swing of both TFTs is ~0.1 V $decade^{-1}$.
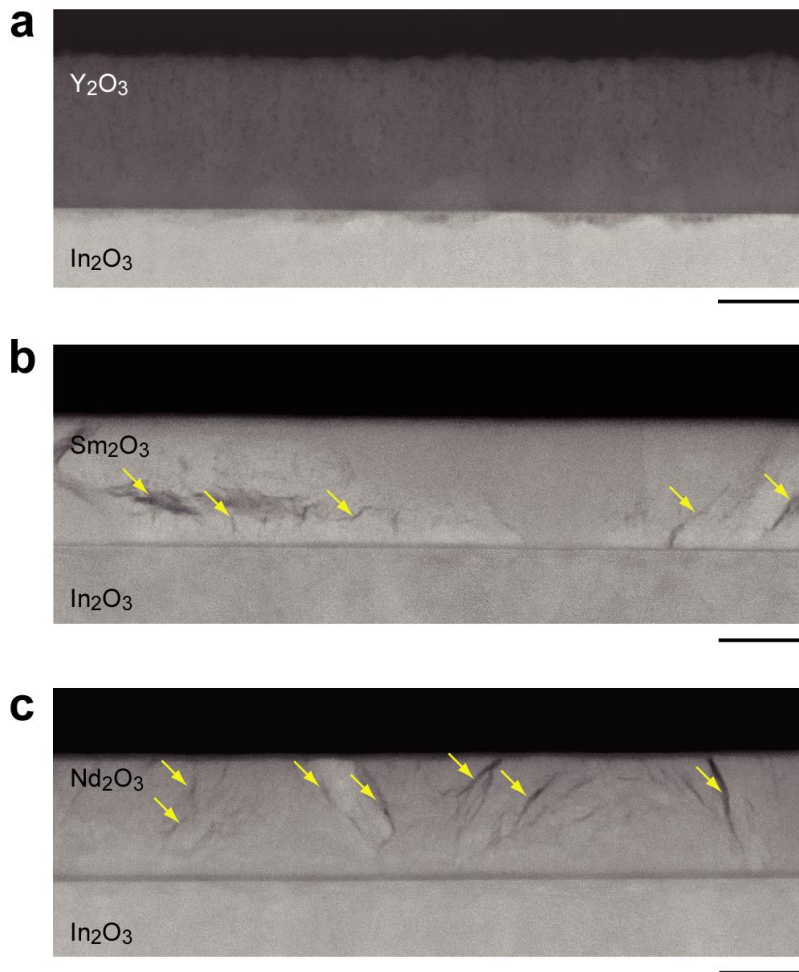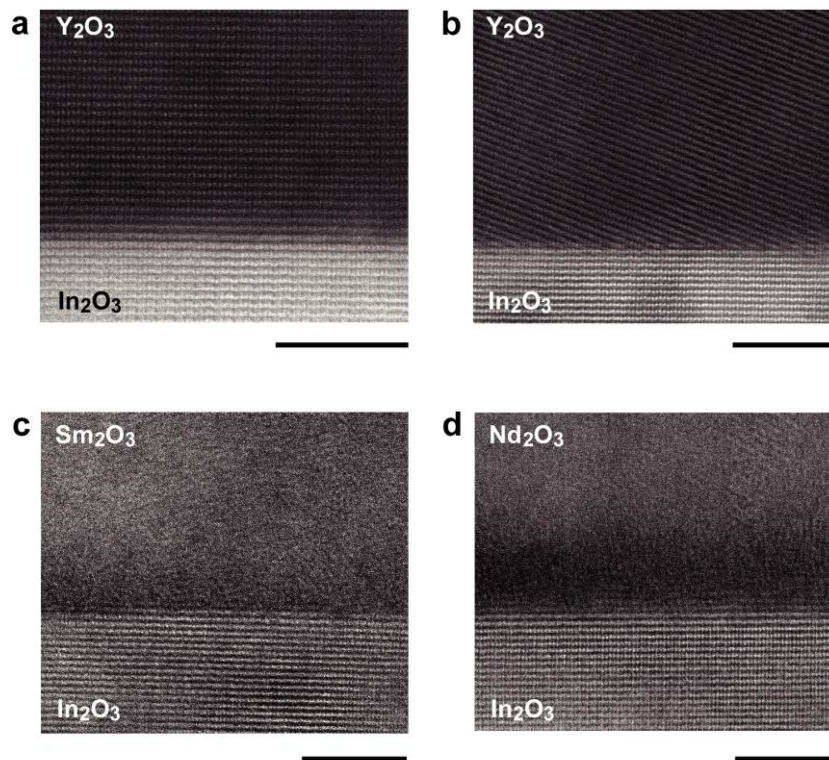
Figure 4: Cross-sectional HAADF-STEM images of the *Ln*$_2$O$_3$ films on (111)-oriented In$_2$O$_3$ epitaxial films (10%-Sn-doped).

(a) Y$_2$O$_3$ (C-rare earth), (b) Sm$_2$O$_3$ (B-rare earth), and (c) Nd$_2$O$_3$ (A-rare earth). The yellow arrows indicate the cracks. No cracks are observed in the Y$_2$O$_3$ film, while many cracks are observed in the Sm$_2$O$_3$ and Nd$_2$O$_3$ films. The incident e-beam direction is $\langle 1\bar{1}0 \rangle$ In$_2$O$_3$. The scale bars are 50 nm.

Figure 5: Cross-sectional HAADF-STEM images (magnified) of the *Ln*₂O₃ films on (111)-oriented In₂O₃ epitaxial films (10%-Sn-doped).

(a, b) Y_2O_3 (C-rare earth), (c) Sm_2O_3 (B-rare earth), and (d) Nd_2O_3 (A-rare earth). Lattice structures are observed in the case of Y_2O_3 film along with In_2O_3 lattice, indicating that heteroepitaxial growth occurs on the In_2O_3 crystal. In contrast, lattice structure is not observed in the case of Sm_2O_3 and Nd_2O_3 films. Further, thin amorphous layers are observed at the heterointerfaces of Sm_2O_3/In_2O_3 and Nd_2O_3/In_2O_3. The incident e-beam direction is $<1\bar{1}0>$ In_2O_3. The scale bars are 5 nm.
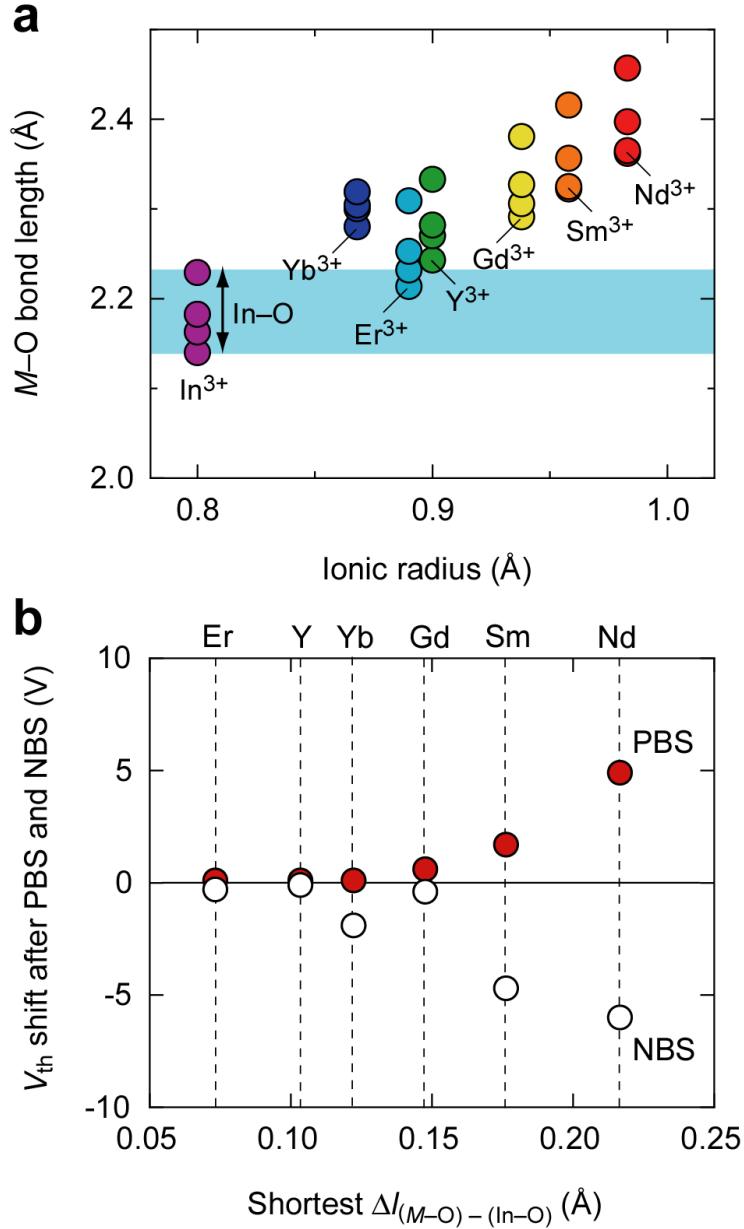
Figure 6: Possible mechanism of suppression of bias stress shift.
(a) Relationship between the ionic radius and metal−oxygen bond (M−O) length in various Ln_2O_3. The M−O length linearly increases with the expanding ionic radius of the metal. The light blue indicates the In−O length range. (b) V_{th} shifts after PBS and NBS of the In_2O_3 TFTs as a function of the difference in M−O length from In−O length ($\Delta l_{(M-O) - (In-O)}$). The $\Delta l_{(M-O) - (In-O)}$ of the Ln_2O_3 were extracted from **Fig. 6a**. The V_{th} shifts are significant for both PBS and NBS when the shortest $\Delta l_{(M-O) - (In-O)}$ of the passivation layer exceeds 0.15 Å (Gd_2O_3). In contrast, the V_{th} shifts are negligible when the shortest $\Delta l_{(M-O) - (In-O)}$ is below 0.10 Å (Y_2O_3).

17

Supplementary Information

Reliable operation in high-mobility indium oxide thin film transistors

Prashant R. Ghediya, Yusaku Magari*, Hikaru Sadahira, Takashi Endo, Mamoru Furuta, Yuqiao Zhang, Yasutaka Matsuo & Hiromichi Ohta*
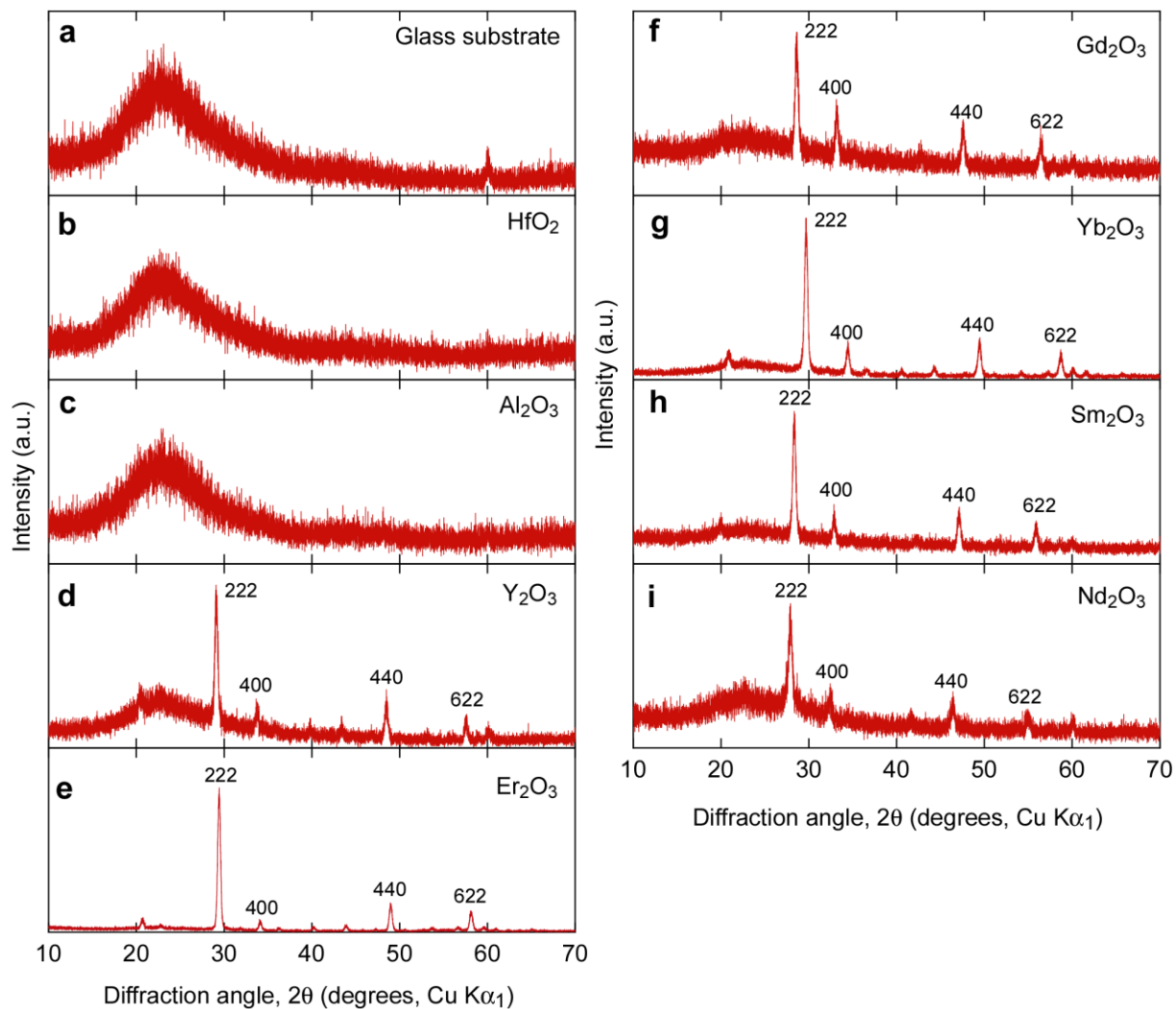
Figure S1: XRD patterns of the passivation layers after thermal annealing at 370 °C.
The incident angle of the X-ray is 0.5°. (a) Glass substrate, (b) HfO_2, (c) Al_2O_3, (d) Y_2O_3, (e) Er_2O_3, (f) Gd_2O_3, (g) Yb_2O_3, (h) Sm_2O_3, and (i) Nd_2O_3. The passivation layers (100 nm) were deposited on alkali-free glass substrates and then thermally annealed at 370 °C in air. After the thermal annealing, Ln_2O_3 films were polycrystalline whereas HfO_2 and Al_2O_3 films remained amorphous.
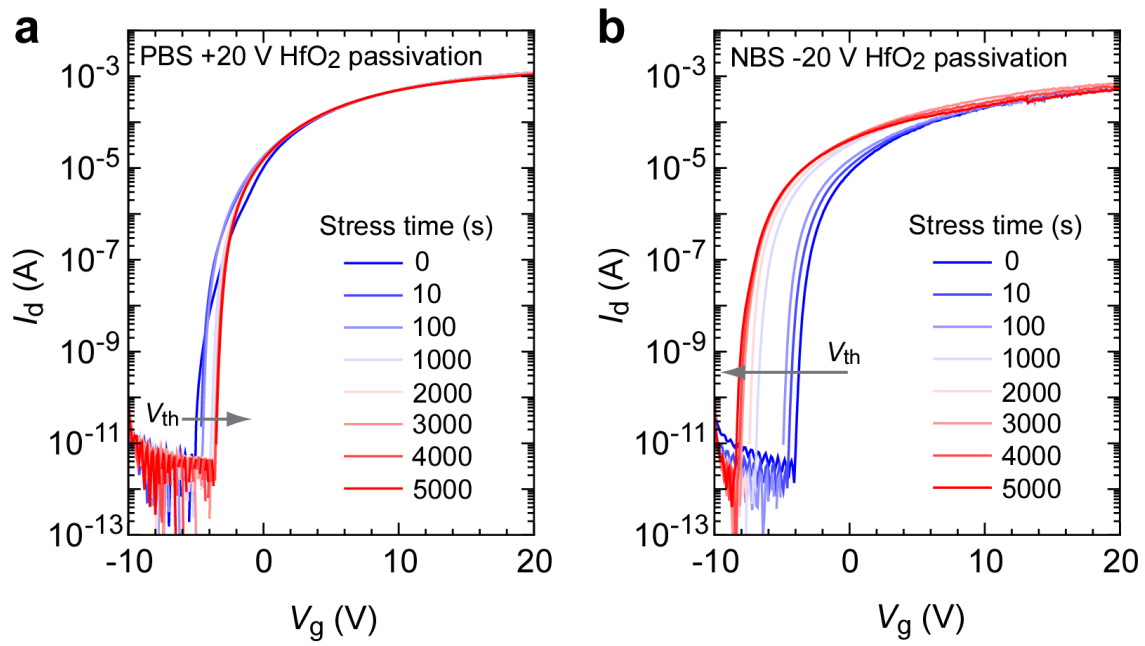
Figure S2: Bias stress test results of the In$_2$O$_3$ TFT passivated with a HfO$_2$ film.
Changes in transfer characteristics under (a) PBS (+20 V) and (b) NBS (−20 V). Threshold
voltage (V_{th}) shifts of +1.2 V after 5000 s PBS and −4.4 V after 5000 s NBS are observed,
indicating that the HfO$_2$ film is not effective as the passivation layer for In$_2$O$_3$ TFTs.
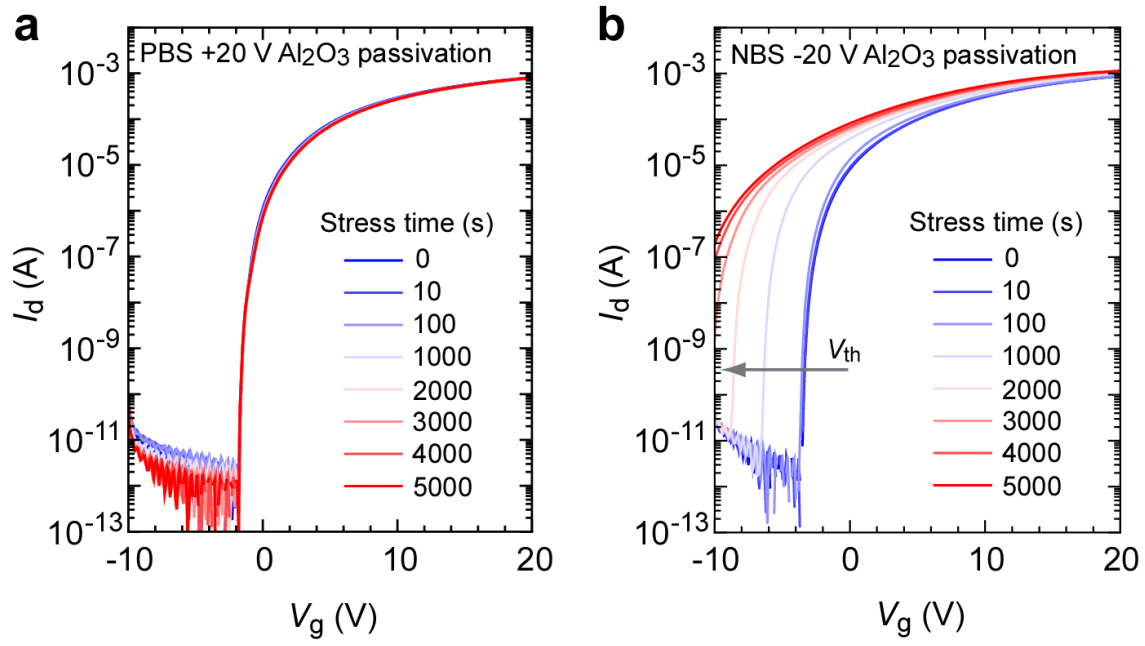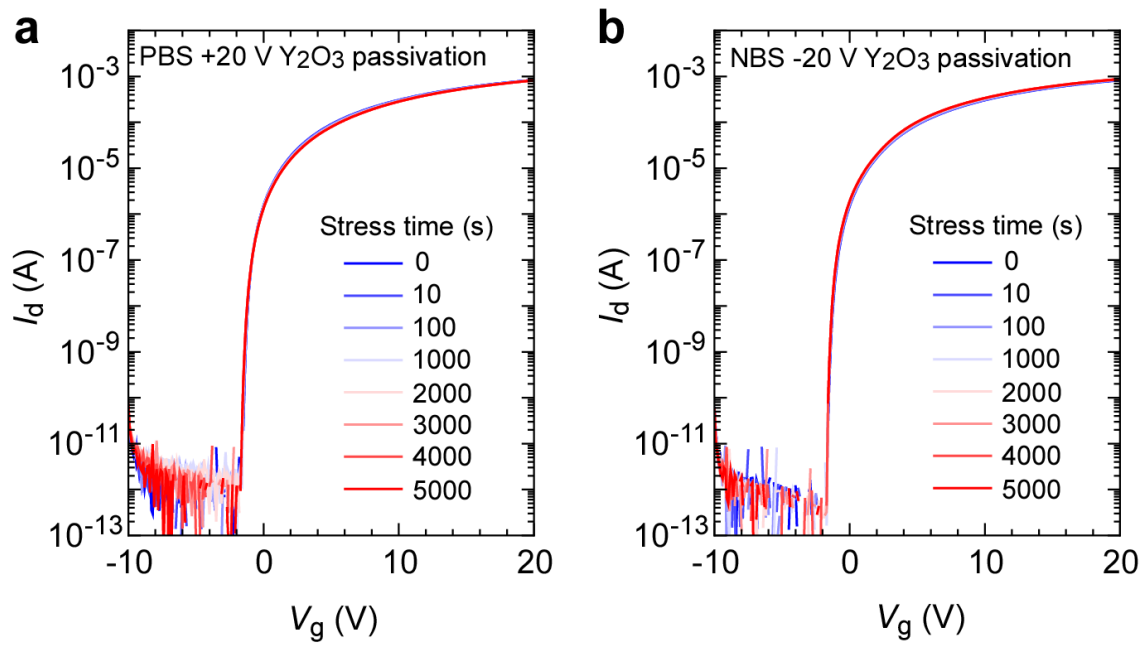
Figure S3: Bias stress test results of the In$_2$O$_3$ TFT passivated with an Al$_2$O$_3$ film.
Changes in transfer characteristics under (a) PBS (+20 V) and (b) NBS (−20 V). Threshold
voltage (V_{th}) shifts of +0.9 V after 5000 s PBS and −7 V after 5000 s NBS are observed,
indicating that the Al$_2$O$_3$ film is not effective as the passivation layer for In$_2$O$_3$ TFTs.

Figure S4: Bias stress test results of the In_2O_3 TFT passivated with a Y_2O_3 film.
Changes in transfer characteristics under (a) PBS (+20 V) and (b) NBS (−20 V). The
threshold voltage (V_{th}) shifts after 5000 s of PBS and 5000 s of NBS were negligible,
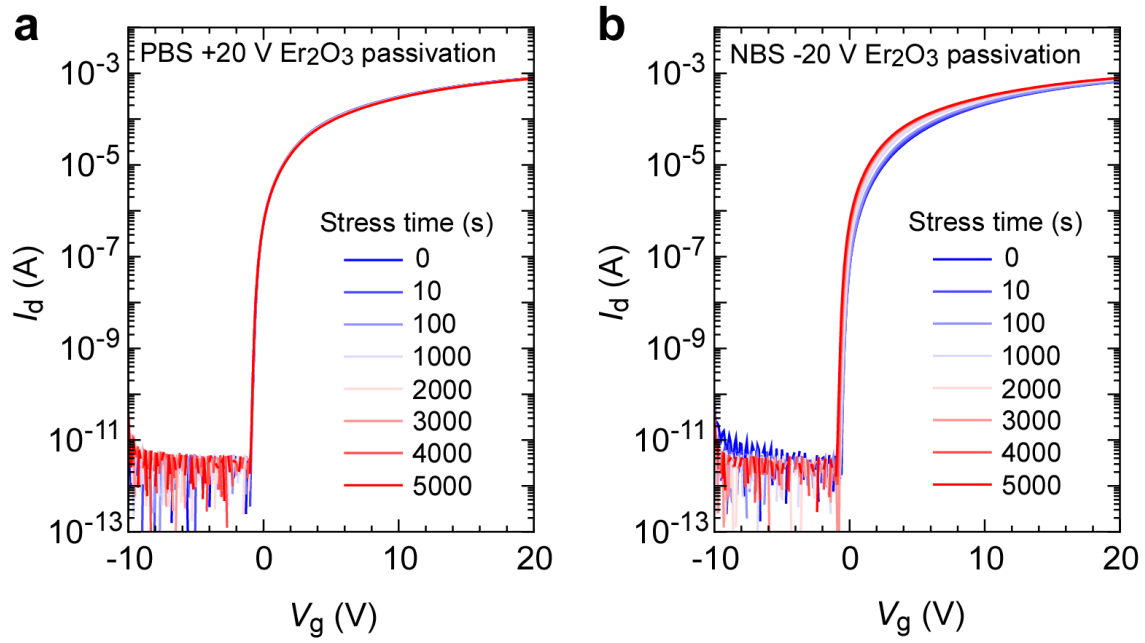indicating the high reliability of the In_2O_3 TFT passivated with the Y_2O_3 film.
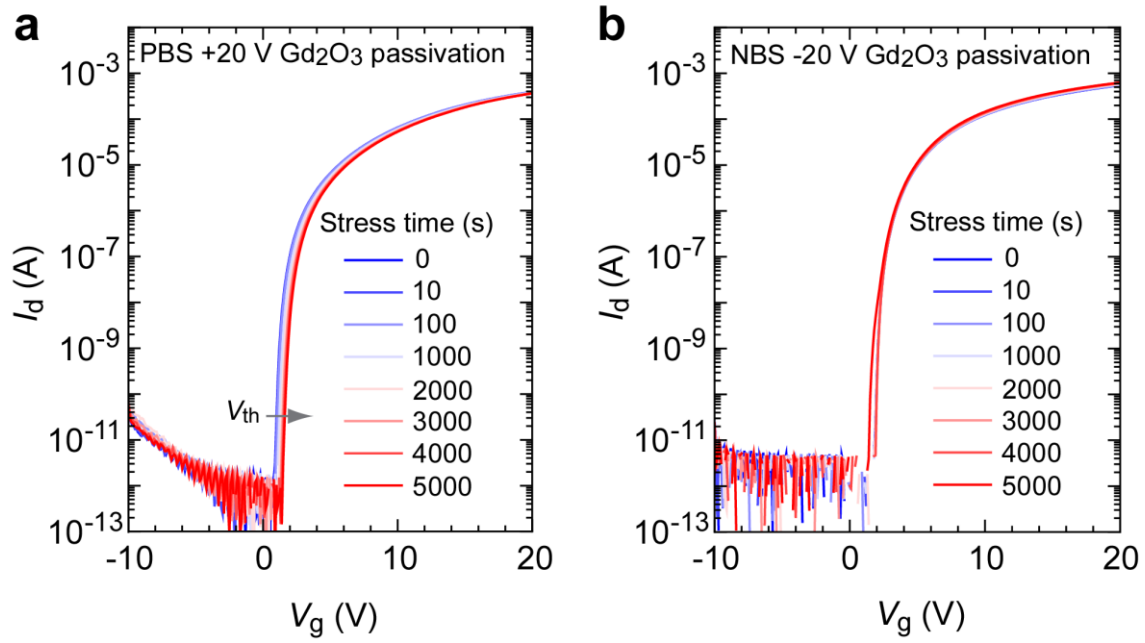
Figure S5: Bias stress test results of the In$_2$O$_3$ TFT passivated with an Er$_2$O$_3$ film.
Changes in transfer characteristics under (a) PBS (+20 V) and (b) NBS (−20 V). The threshold voltage (V_{th}) shifts after 5000 s of PBS and 5000 s of NBS were negligible, indicating the high reliability of the In$_2$O$_3$ TFT passivated with the Er$_2$O$_3$ film.

Figure S6: Bias stress test results of the In$_2$O$_3$ TFT passivated with a Gd$_2$O$_3$ film.
Changes in transfer characteristics under (a) PBS (+20 V) and (b) NBS (−20 V). The Gd$_2$O$_3$ film passivation results in a +0.6 V V_{th} shift after the PBS, whereas it results in a small V_{th} shift (−0.4 V) after the NBS.
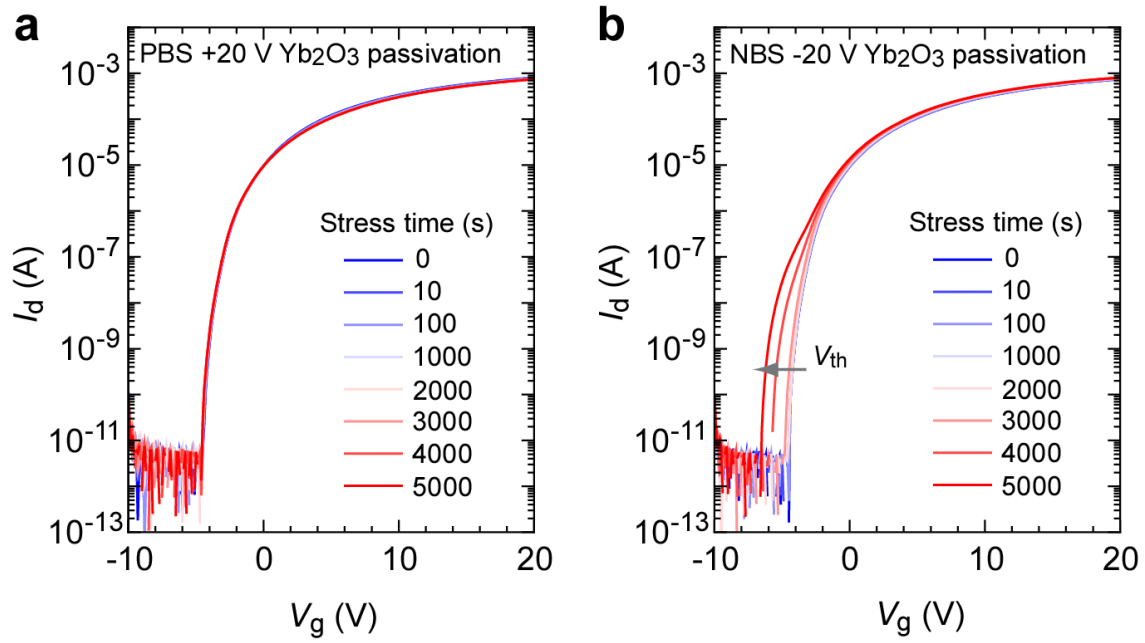
Figure S7: Bias stress test results of the In_2O_3 TFT passivated with a Yb_2O_3 film.
Changes in transfer characteristics under (a) PBS (+20 V) and (b) NBS (−20 V). The Yb_2O_3 film passivation results in a negligible V_{th} shift after the PBS, whereas it results in a rather large V_{th} shift (−1.9 V) after the NBS.
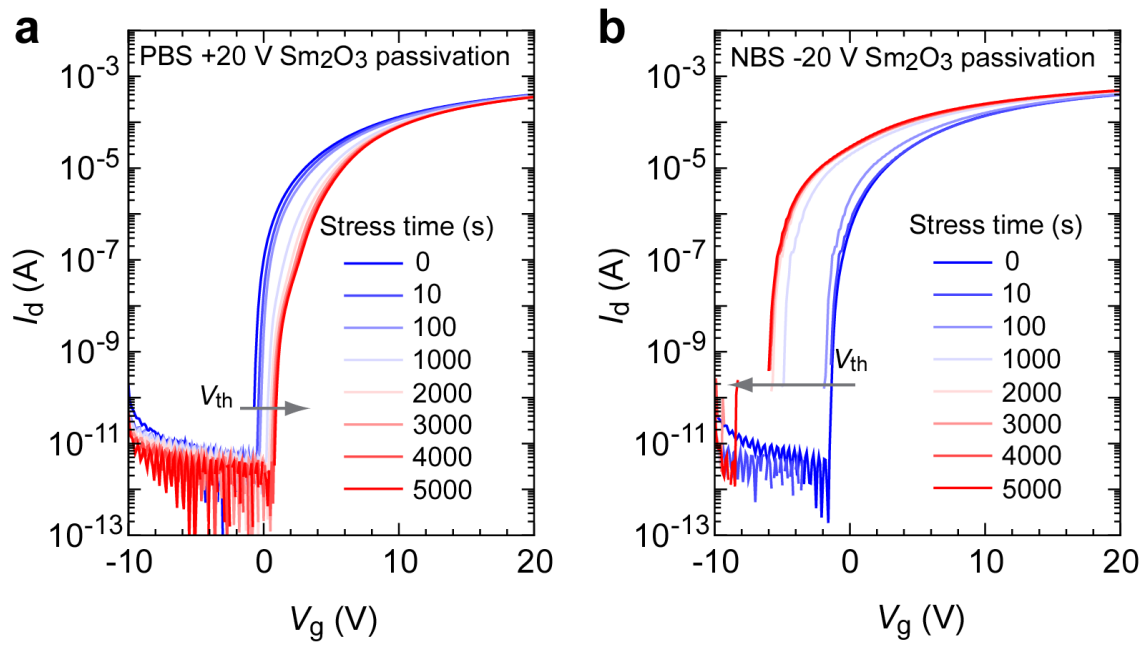
Figure S8: Bias stress test results of the In$_2$O$_3$ TFT passivated with a Sm$_2$O$_3$ film.
Changes in transfer characteristics under (a) PBS (+20 V) and (b) NBS (−20 V). Threshold
voltage (V_{th}) shifts of +1.7 V after 5000 s PBS and −4.7 V after 5000 s NBS are observed,
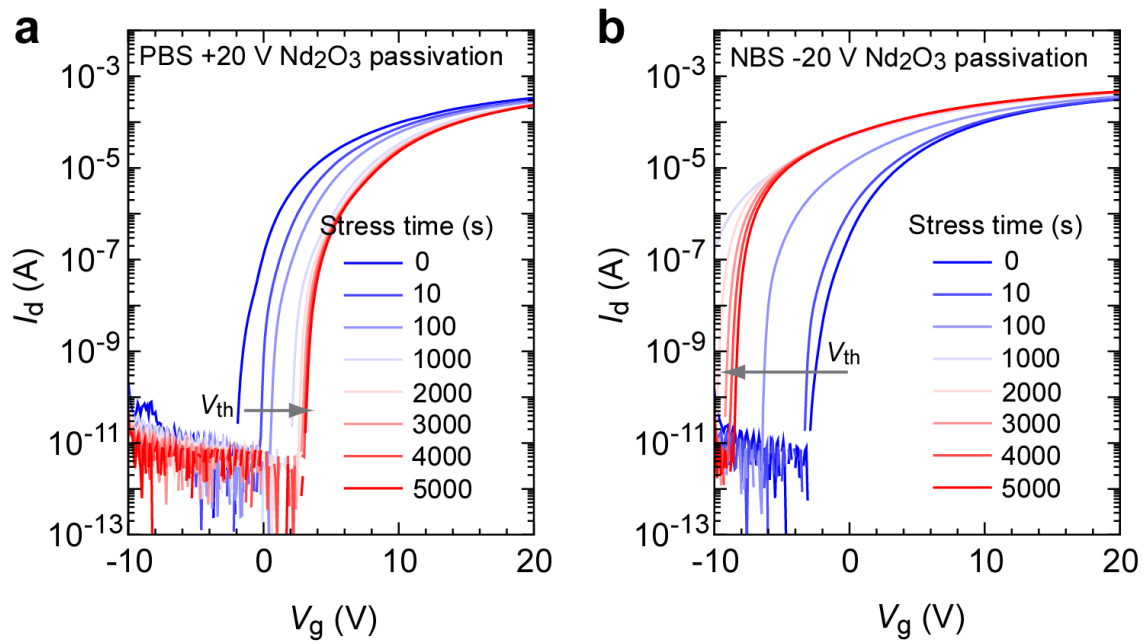indicating that the Sm$_2$O$_3$ film is not effective as the passivation layer for In$_2$O$_3$ TFTs.

Figure S9: Bias stress test results of the In₂O₃ TFT passivated with a Nd₂O₃ film.
Changes in transfer characteristics under (a) PBS (+20 V) and (b) NBS (−20 V). Threshold voltage (V_{th}) shifts of +4.9 V after 5000 s PBS and −6 V after 5000 s NBS are observed, indicating that the Nd₂O₃ film is not effective as the passivation layer for In₂O₃ TFTs.
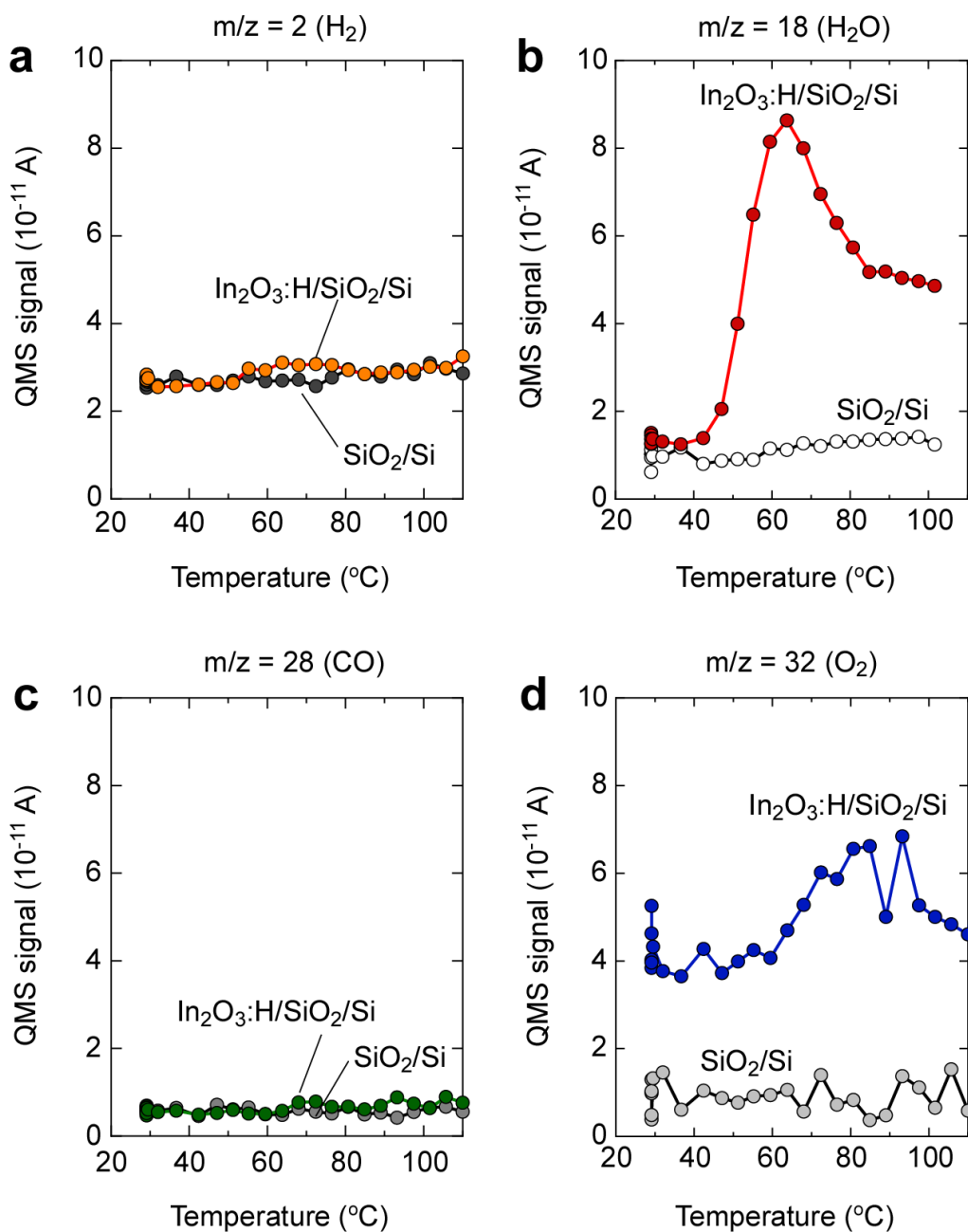
Figure S10: Thermal desorption spectroscopy of In₂O₃ films.
(a) $m/z = 2$ (H_2), (b) $m/z = 18$ (H_2O), (c) $m/z = 28$ (CO), and (d) $m/z = 32$ (O_2). A SiO_2/Si substrate was also tested. Large desorption peaks of H_2O and O_2 are observed around 60 °C and 80 °C, respectively, whereas the desorption of H_2 and CO is negligibly small.

Table S1: Comparison of reliability of In_2O_3 TFTs with various passivation layers.

Passivation	Structure	PBS (V)	NBS (V)	Judgment
Without	—	+1.0	–10.0	poor
HfO_2	Amorphous	+1.2	–4.4	poor
Al_2O_3	Amorphous	+0.02	–7.0	poor
Y_2O_3	Polycrystalline (C-rare earth)	+0.1	–0.1	excellent
Er_2O_3	Polycrystalline (C-rare earth)	+0.1	–0.3	excellent
Gd_2O_3	Polycrystalline (C-rare earth)	+0.6	–0.4	excellent
Yb_2O_3	Polycrystalline (C-rare earth)	+0.1	–1.9	fair
Sm_2O_3	Polycrystalline (B-rare earth)	+1.7	–4.7	poor
Nd_2O_3	Polycrystalline (A-rare earth)	+4.9	–6.0	poor